Article

A Widely and Continuously Tunable Single-Mode Transmitter Based on a Hybrid Microcavity Laser

Miao-Qing Wang [1,2], **Bin Zhang** [2], **Zhen-Ning Zhang** [3,4], **You-Zeng Hao** [3,4], **Zun-Hao Hu** [3,4], **Yue-De Yang** [3,4], **Jin-Long Xiao** [3,4,*], **António L. Teixeira** [1] and **Yong-Zhen Huang** [3,4]

[1] Departamento de Eletónica, Telecomunicações e Informática (DETI), Instituto de Telecomunicações, University of Aveiro, 3810-193 Aveiro, Portugal; james.wang@zktel.com.cn (M.-Q.W.); teixeira@ua.pt (A.L.T.)

[2] Shaoxing ZKTEL Equipment Co., Ltd., Shaoxing 312000, China; bin.zhang@zktel.com.cn

[3] Center of Materials Science and Optoelectronics Engineering, University of Chinese Academy of Sciences, Beijing 100049, China; zzn@semi.ac.cn (Z.-N.Z.); haoyouzeng@semi.ac.cn (Y.-Z.H.); huzunhao@semi.ac.cn (Z.-H.H.); yyd@semi.ac.cn (Y.-D.Y.); yzhuang@semi.ac.cn (Y.-Z.H.)

[4] Key Laboratory of Optoelectronic Materials and Devices, Institute of Semiconductors, Chinese Academy of Sciences, Beijing 100083, China

[*] Correspondence: jlxiao@semi.ac.cn

Abstract: A method for achieving the single-mode and efficient unidirectional emission of a whispering gallery mode (WGM) semiconductor laser is presented herein. Hybrid square-rectangular lasers (HSRLs) and hybrid square/rhombus-rectangular lasers (HSRRLs) consisting of a Fabry–Pérot (FP) cavity and a square or rhombus cavity microcavity are described. In addition, a transmitter optical subassembly (TOSA) based on an HSRRL chip was fabricated, which has a wide and continuous wavelength tuning range. Wavelength channels from 1555.75 nm to 1568.15 nm with a spacing of 50 GHz were demonstrated with a good side mode suppression ratio (SMSR) and good output power. These devices have the potential to meet the typical requirements of optical communication networks.

Keywords: whispering gallery mode; microcavity; semiconductor lasers; transmitter optical subassembly

1. Introduction

Whispering gallery mode (WGM) optical microcavities are types of light-confining dielectric structures with high quality (*Q*) factors, small mode volumes, and a capacity for planar integration. Optical microcavities of various shapes on the wavelength scale have been developed based on WGM, such as spherical [1,2], micro-disk [3–7], micro-ring [8–10], and polygon cavities [11]. Semiconductor lasers based on WGM cavities have the potential to achieve low thresholds and low power consumption due to the advantages of WGM cavities. Microdisk semiconductor lasers were first demonstrated in 1992 [12], and room-temperature microcylinder semiconductor lasers in 1993 [13]. Since then, WGM microcavity lasers have been extensively studied [14–23]. Nevertheless, isotropic emission is an obvious shortcoming of conventional WGM microcavities, which limits the emission efficiency of lasers [24]. Optimizing the cavity shape [25–27] or adding local perturbations to the cavity, such as notches [28], are common approaches to breaking isotropic emission.

The hybrid cavity is a mode-controllable structure that works by coupling multiple cavities and easy to operate single-mode, which has been developed for decades to be applied to monolithic semiconductor lasers, such as cleaved-coupled cavities [29], V-coupled cavities [30,31], double-ring cavities [32,33], two-section Fabry–Pérot (FP) cavities [34], and multimode interference hybrid cavities [35]. In addition, hybrid cavity structures facilitate the realization of wavelength-tunable devices based on a square microcavity connected with an FP cavity [36]. Industrial-grade 25 Gb/s wavelength division multiplexing (WDM) lasers have been proposed for 5G network systems [37,38]. Wavelength-tunable technology

is important in optical communication systems, especially for DWDM. Lasers with a wide tuning capability, covering the C-band and even the L-band, can be a lower-cost alternative to fixed wavelength lasers of different channels, thus reducing the inventory cost of DWDM lasers. In addition, the next-generation passive optical network stage 2 (NG-PON2) features multiwavelength channels, in which tunable transceiver technology is widely demanded in subscriber optical network units (ONUs) [39]. In addition to hybrid cavity lasers, a variety of tunable lasers with different structures have been developed, such as external cavity lasers (ECLs) [40], DFB laser arrays [41], and DBR lasers [42,43].

In this paper, we provide a review of a hybrid cavity semiconductor laser composed of a square cavity directly coupled to an FP cavity, which retains the high-Q coupled mode and efficient unidirectional output. Single-mode operation is realized by hybrid square-rectangular lasers (HSRLs) [36] and hybrid square/rhombus-rectangular lasers (HSRRLs) [44,45]. An optical transmitter based on an HSRRL was fabricated that has a more compact structure, lower fabrication cost, and good tuning performance.

A square microcavity is mainly presented as a WGM cavity; the corresponding mode theory and unidirectional emission method are numerically analyzed in Section 2. To obtain a single-mode output light, we extended the output waveguide as an FP cavity; that an HSRL consists of a square cavity and an FP cavity is introduced in Section 3. In Section 4, we present the development of a hybrid square/rhombus-rectangular laser, a modified square-rectangular cavity. In Section 5, we discuss packaging the laser chip to industrialize and commercialize the potential chip. Conclusions are summarized in Section 6.

2. Square Microcavity

The mode theory of square cavities has been extensively studied. The three-dimensional (3D) square cavity can be simplified to a two-dimensional (2D) model with the effective refractive index approximation method. Group theory is used to analyze the symmetry of a square geometry, and Marcatili's approximate solution based on Maxwell's equations is used to calculate mode analytic solutions, which are sufficiently accurate inside the microcavity and at the boundaries, except for four vertices [11]. The transverse electric (transverse magnetic) eigenmodes in a square microcavity are denoted as $TE_{p,q}$ ($TM_{p,q}$), where p and q are the node numbers of the waves in the two orthogonal directions. The degeneration of $TE_{p,q}$, and $TE_{q,p}$ are obvious due to the symmetry of the square, and the coupling between the two degenerate modes produces high-Q WGMs, which can be classified into transverse modes with node number $m = |p - q|/2 - 1$, and longitudinal modes with node number $l = p + q$.

Here, a 2D model of a square microcavity with a side length of 10 μm is simulated. The cavity consists of InP with an effective refractive index of 3.2 and is surrounded by benzocyclobutene (BCB) with an index of 1.54. WGMs with a wavelength of around 1550 nm are calculated numerically by solving the eigenvalues, and the corresponding Q factors are estimated using the finite element method (FEM). Figure 1 shows the Q factors of TE and TM modes with different transverse and longitudinal mode orders. The simulation result shows that the lower the transverse mode orders m, the higher the mode Q factor. The free spectral range (FSR) of the TE modes is about 52.6 nm, which is related to the wavelength interval between $TE_{29,27}$ and $TE_{30,28}$ as the adjacent longitudinal modes. Figure 2 shows the intensity distributions of the fundamental mode $TE_{29,27}$ and the first-order mode $TE_{30,26}$, whose l are both 56, and m are 0 and 1, respectively.

Compared to traditional DFB lasers, WGM lasers are competitive in terms of their high Q factor. However, isotropic emission is an obvious shortcoming of the traditional WGM microcavity. Due to the high degree of symmetry of the geometry, it is difficult to achieve unidirectional output from a square microcavity, which limits laser efficiency and output power.
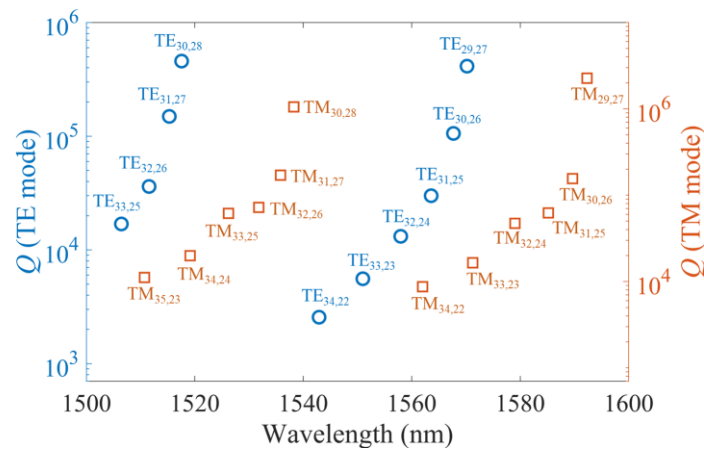
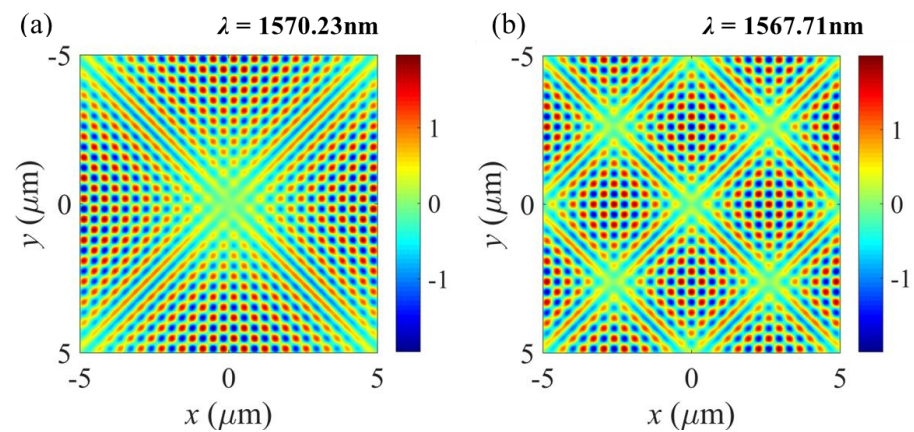**Figure 1.** Q factors of TE and TM modes with a square cavity around 1550 nm.

Figure 2. Intensity distributions of (**a**) the fundamental mode $TE_{29,27}$ and (**b**) the first-order mode $TE_{30,26}$.

An output waveguide butt-coupled to the square cavity can be used to realize unidirectional emission [11]. Many reports have been made regarding the fabrication of such a waveguide-coupled square cavity laser without degrading the mode Q factor. Several coupling schemes based on the envelope node position of the mode distribution were proposed and calculated. Simulation results confirm that coupling at the vertex of the square cavity, where the envelope node of all WG-like modes is located, minimally affects mode distributions and enables efficient coupling between WG-like modes and FP modes [11]. The 3D square microcavity is more complicated than the 2D microcavity, and the vertical radiation loss is not negligible in the 3D configuration. In addition, coupling with a waveguide breaks the symmetry of the square cavity, and the coupling position has a significant impact on the coupling efficiency of different modes.

3. Hybrid Square-Rectangular Laser

Square microcavities usually operate in multiple modes, which is detrimental to long-distance optical communications. The output waveguide is extended to about 300 μm to realize single-mode lasers acting as an FP cavity. A hybrid cavity is proposed that couples a square microcavity with an FP cavity. The coupling position is at the vertex of a square cavity, which has been confirmed to have the least influence on WGMs, as mentioned above. The mode coupling of such a hybrid square-rectangular laser (HSRL) is described by Ma et al. in [36]. Within the same gain spectral range, the WGM cavity usually operates with a single longitudinal mode due to its short cavity length and large FSR of around 50 nm, while a conventional FP cavity with a cavity length of 200~300 μm instead operates with a multi-longitudinal mode. A wavelength-tunable hybrid mode was generated to

couple square WGMs and FP modes, as the diagram in Figure 3 shows. The square cavity is regarded as a wavelength-selective resonant reflector at the end face of the FP cavity, whose reflection spectrum and mode field are determined by the structure parameters.
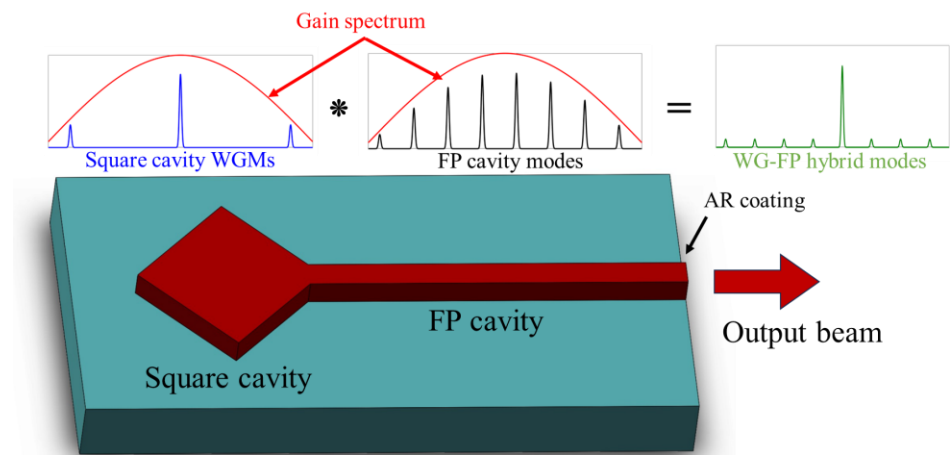

Figure 3. Schematic diagram of HSRL.

A 2D model of the HSRL with a square side length a = 10 μm, FP cavity length L = 300 μm, and width d = 2 μm was numerically simulated to be made of InP and surrounded by BCB, with the equivalent refractive indexes of InP and BCB set to 3.2 and 1.54, respectively. The simulations were carried out using the finite-difference time-domain (FDTD) method. A time-domain source excited the TE mode in the FP cavity, and the photonic signal reflected from the square cavity was monitored. The mode spectrum of the hybrid modes was derived from the reflected signal at a steady state when low-quality modes were dissipated, and processed by the Pade approximation and Fourier transform [11], as shown in Figure 4. The peaks of the curve appeared at 1559.5 nm, 1556.5 nm, and 1551.9 nm, indicating the high Q modes of different orders, and the FSR of the hybrid modes was about 51 nm, corresponding to the parameters of the square cavity. In the steady state, the magnetic amplitude H_z distributions of the fundamental mode and the first-order mode are shown in Figure 5a,c. The hybrid modes were not identical to the WGMs compared to Figure 2a,b. The WG-like modes were a combination of the two cavity modes. Figure 5b,d show the k-space mode distribution (p, q) of the fundamental mode and the first-order mode, respectively, where p and q denote the wave numbers in the x and y directions, respectively. The fundamental mode at 1559.5 nm consisted of (28, 30) and (27, 31), which were square modes, and (29, 29), which was a waveguide mode pointing towards the FP cavity. Similar to the fundamental mode, the first-order mode at 1556.5 nm consisted of (28, 32), (27, 33), and (30, 30).
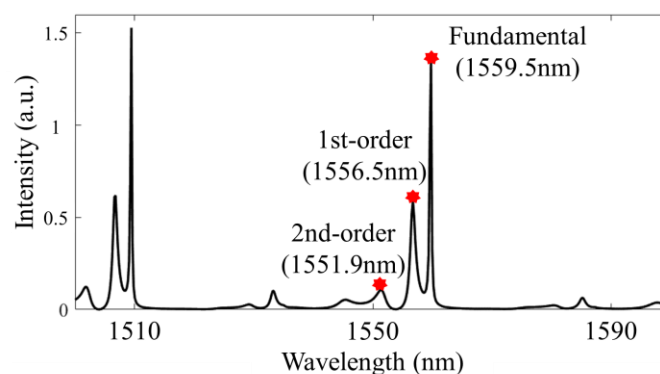

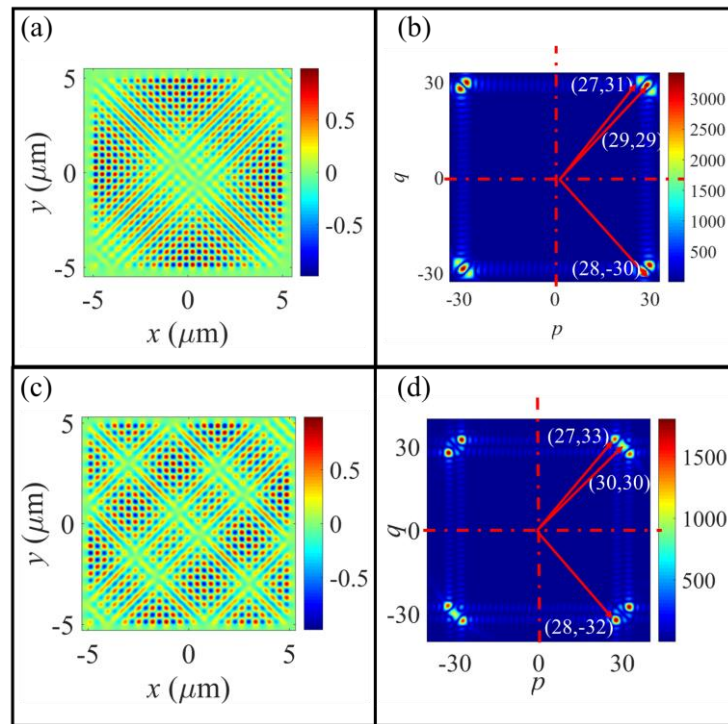**Figure 4.** The mode spectrum of the hybrid mode.

Figure 5. The H_z distribution of the TE fundamental WG-like mode in (**a**) coordinate-space and (**b**) *k*-space, and of the 1st-order WG-like mode in (**c**) coordinate-space and (**d**) *k*-space.

The HSRL was fabricated, and the relative intensity noise, frequency noise, and linewidth were characterized. In the experiment, injection currents I_{FP} and I_{SQ} were provided for the two microcavities. The optical output of the HSRL was coupled into a single-mode fiber (SMF). By adjusting I_{FP} and I_{SQ}, the wavelength of the hybrid mode shifted due to the heating effect and free carrier dispersion. Under the specific injection current, stable single-mode operation was realized, with a good SMSR of about 40 dB, and a narrow linewidth of around 2.9 MHz [46]. However, the *P–I* curve was not smooth, because the mode hopping phenomenon can easily occur when the high-*Q* fundamental WG-like mode is coupled with FP modes. The FP modes in a square-rectangular hybrid cavity are a mixture of the fundamental transverse mode and a large proportion of high-order symmetric modes, which degrades the far-field radiation characteristics and the coupling efficiency of an SMF. An optimized design is required to realize a stable and tunable single-mode laser.

4. Hybrid Square/Rhombus-Rectangular Laser

Deep etching of the HSRL preserves the high-*Q* WGMs in the square cavity, but generates high-order transverse modes that occupy a large fraction in the FP cavity. The fundamental transverse mode fraction, termed *η*, can be obtained from the overlap integral between the FP fundamental transverse modes and the hybrid modes. The reduction of *η* increases mode hopping and reduces the coupling efficiency of the laser to an SMF. To improve *η* in the FP cavity, Hao et al. proposed a hybrid square/rhombus-rectangular laser (HSRRL) consisting of a square/rhombus microcavity (SRM) and an FP cavity [44,45].

4.1. Theory

The SRM is a square cavity with a deformation *δ*, and an FP cavity of length *L* and width *d* is directly connected to the deformed vertex of the SRM, as shown in Figure 6. Theoretically, the deformation of the SRM acts as a transition region between the square cavity and the FP cavity, increasing the loss of higher-order transverse modes in the FP

cavity, thus improving the fundamental mode fraction. The SRM also acts as an equivalent reflector, whose performance at different δ is simulated in [44].
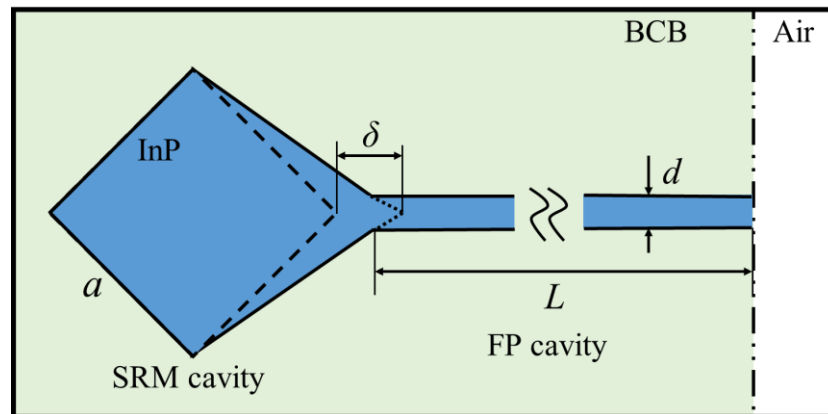

Figure 6. Schematic layout of an HSRRL.

At a specific $\delta = 0.2$ μm, and with the other optimal parameters that $L = 300$ μm and $d = 2$ μm, the mode pattern of the z-direction magnetic field H_z is calculated. Figure 7a,b show the intensity distribution of the highest Q modes in HSRL and HSRRL, respectively, including intensity profiles around the output facet of the FP cavity and far-field radiation profiles. According to Figure 7, the hybrid mode with a Q of 12,058 in HSRL consisted of a fundamental WG-like mode and many higher-order FP modes. In comparison, this mode in the HSRRL had a Q factor of 4081. This is because the hybrid modes in the HSRRL combined high-order WG-like modes and fundamental FP modes that broke the perfect symmetry of a square due to the deformation. Figure 7 shows the calculation result that the η of the modes in HSRRL was over 90%, which was much higher than the modes in HSRL of about 35%. The innovative design of HSRRL significantly improved far-field radiation characteristics, which is beneficial for the coupling efficiency of an SMF.
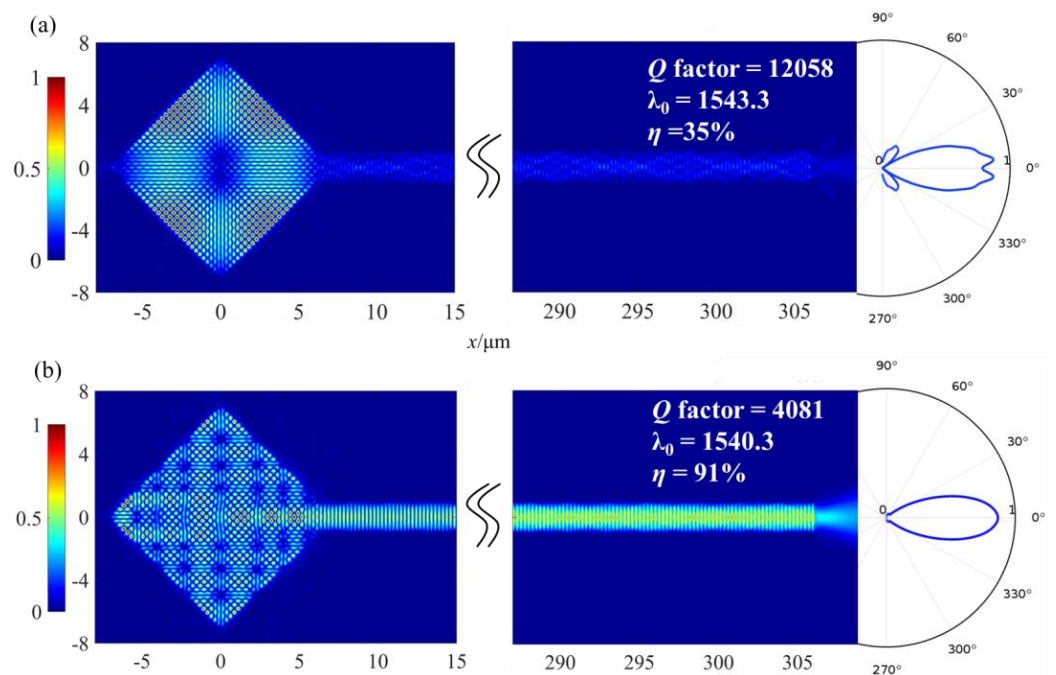

Figure 7. Simulated mode intensity profiles around the output facet and far-field intensity profiles of (**a**) HSRL and (**b**) HSRRL with the deformation $\delta = 0.2$ μm.

4.2. Experiment

An AlGaInAs/InP epitaxial wafer on an n-doped InP substrate was used to fabricate an HSRRL, with the AlGaInAs active layer consisting of compressively strained multiple quantum wells (MQWs). The AlGaInAs MQWs layer provided gain that performed well at high temperatures due to its good confinement of electrons. The process can be roughly divided into four steps using contacting photolithography and inductively coupled plasma (ICP) etching techniques [47]. First, the SiO$_2$ mask layer is deposited on the AlGaInAs/InP wafer, where the pattern of the hybrid cavity is formed and transferred to the wafer by ICP etching. To obtain a high-Q WGM, the etch depth should be deeper than 4 μm, which crosses the active region. The pattern of the hybrid cavity is laterally surrounded by a 200 nm SiN$_x$ layer to prevent injection current leakage, and a BCB confinement layer is deposited to flatten the surfaces. Second, an electrical isolation trench between the WGM and FP cavities is etched on the ohmic contact layer. Third, a SiO$_2$ layer is deposited with the electrical injection window etched on the ohmic contact layer. Finally, the Ti/Pt/Au P-electrodes are patterned separately for the FP and WGM cavities by electron beam evaporation and lift-off. The N-side of the wafer is polished and thinned to about 120 μm, and an Au/Ge/Ni layer is deposited by magnetron sputtering. The microscope image of the HSRRL chip is shown in the inset of Figure 8a, whose size after cleavage is 270 μm × 350 μm. And pad 1 and pad 2 are the P-electrodes of the FP and the SRM cavity, respectively, whose injection currents are noted as I_{FP} and I_{SRM}, respectively. Compared to conventional distributed feedback (DFB) lasers and distributed Bragg reflector (DBR) lasers, the manufacturing process of HSRRL is less expensive because there is no need for grating etching or epitaxial regrowth.
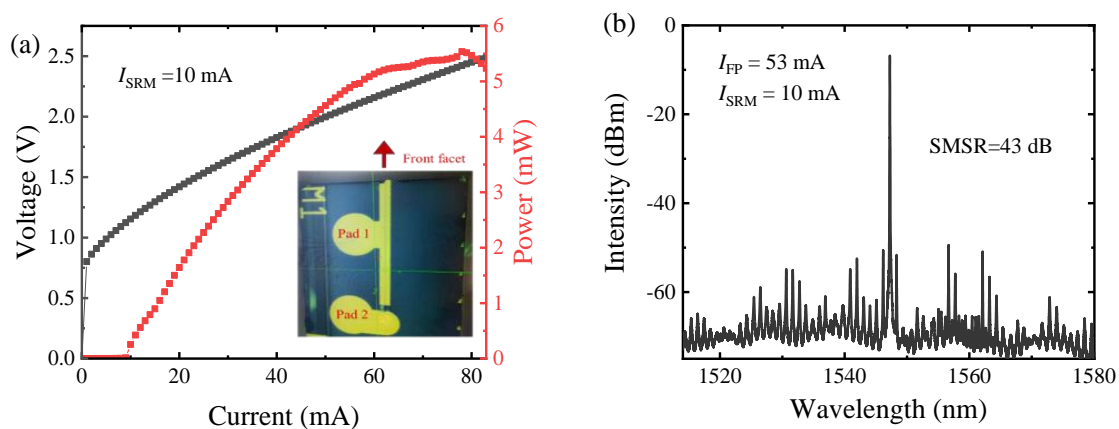

Figure 8. Characteristics of the HSRRL bare chip with (**a**) *P–I–V* curves with a fixed injection current of I_{SRM} and (**b**) spectrum with injection currents of I_{FP} = 53 mA and I_{SRM} = 10 mA. Inset: microscope image of the fabricated HSRRL chip.

The laser characteristics of a laser chip, including *P–I–V* curves and the optical spectrum, were measured when the ambient temperature was 15 °C, and the optical output power was received through a multimode fiber. The *P–I* curves show some kinking due to mode hopping; further research will optimize the resonant cavity structure to reduce mode hopping. Output characteristics under the specific injection currents I_1 and I_2 are shown in Figure 8.

5. Test Results After Packaging

The HSRRL is a novel design that realizes the wavelength-tunable function widely required for next-generation communication technologies such as DWDM, NGPON2, and coherent optical communication. We packaged the HSRRL chip as a transmitter optical subassembly (TOSA) to evaluate its potential for commercial application. The chip was mounted on an AlN submount to form a chip-on-carrier (COC). The COC was then mounted in a hermetic box-can containing a thermoelectric cooler (TEC) for temperature

control. Figure 9a shows a schematic diagram of a nine-pin box package scheme. Pins #3, #4, and #5 are high-speed G-S-G transmission lines with an impedance of 50 ohms, connected to the electrodes of the FP cavity. Pin 6# is connected to the P-electrode of the SRM. The output light from an HSRRL was coupled into an SMF adapter via a square aspherical lens with a maximum coupling efficiency of approximately 47%. Figure 9b shows the finished product.
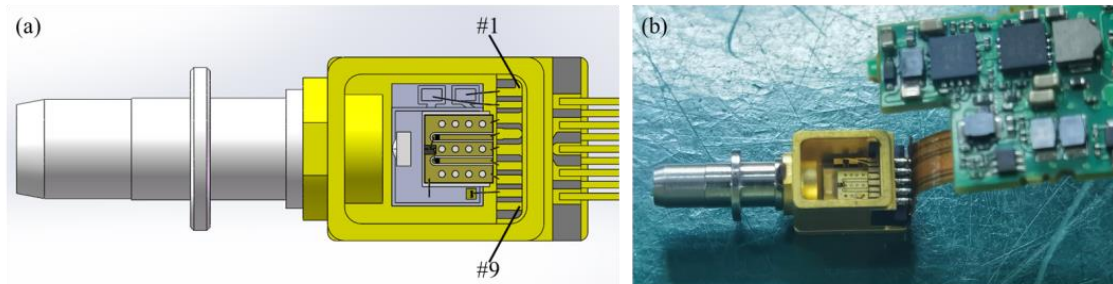

Figure 9. (**a**) Schematic diagram of a nine-pin box packaging scheme and (**b**) the finished product.

The tunable TOSA based on the HSRRL showed good tuning performance in the experiment. The wavelength tunability of the HSRRL is based on the free carrier dispersion of the semiconductor, which changes the refractive index and results in a mode shift, combined with temperature variations due to the injection current. By adjusting the injection current of the FP and SRM cavities, the FP modes and WGMs, respectively, were shifted according to the Vernier effect. However, the heating effect of the injection currents affected the refractive index. During the test process, we controlled the temperature of the COC at 40 °C by TEC. Injection currents I_{FP} and I_{SRM} were applied to pin 5 and pin 8. Figure 10a shows the spectra with a fixed I_{FP} of 40 mA and an adjustable I_{SRM}. As the I_{SRM} increased, the center wavelength of the output beam, which starts at 1555.77 nm, increased at a rate of approximately 0.025 nm/mA, and jumped between the adjacent longitudinal hybrid modes at a wavelength interval of 1.4 nm. The SMSR was measured to be 41.26 dB. Figure 10b shows the spectra with a fixed I_{SRM} of 20 mA and an adjustable I_{FP}. Several modes of WGMs at about 1556.45 nm, 1555.77 nm, 1572.38 nm, and 1572.40 nm were operated in turn and increased continuously at a rate of about 0.033 nm/mA as the I_{FP} increased.
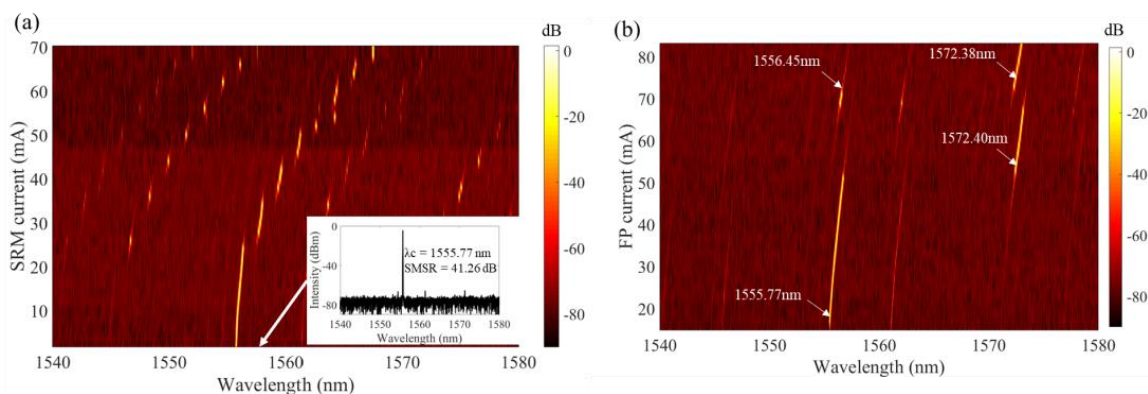

Figure 10. Lasing spectra of the TOSA versus (**a**) I_{SRM} and (**b**) I_{FP}.

A tunable device based on an HSRRL chip provides a wide and continuous tunable wavelength range. We could coarsely tune the wavelength by adjusting the I_{SRM}, and then adjust the I_{FP} and TEC temperature to precisely obtain the required wavelength. The disparity in wavelength tuning accuracy arose from differences in temperature changes due to the varying areas of the SRM and FP cavities. As Figure 11a shows, a 13 nm tuning range

from 1555.75 nm to 1568.15 nm with a wavelength spacing of 50 GHz was realized on the modular level package. Figure 11b shows the corresponding SMSRs and peak intensities of each wavelength channel. During wavelength switching, the TOSA device could maintain a good single-mode laser state in which SMSRs were larger than 35 dB, which satisfied the application requirement. The output intensity fluctuated in the range of −2~3 dBm due to variations in injection currents.
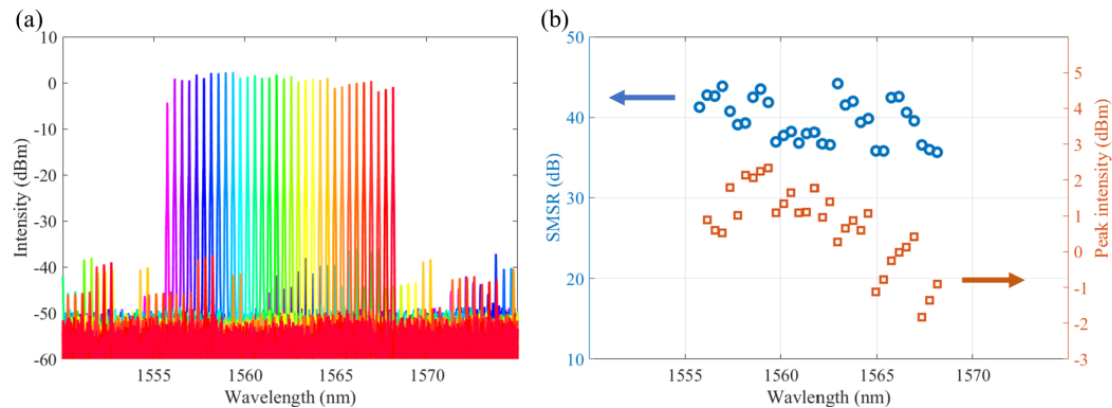

Figure 11. (**a**) Superimposed laser spectra of wavelength channels with a regular interval of 50 GHz and (**b**) SMSRs and peak intensities of each wavelength channel.

6. Conclusions

In conclusion, we introduced the WGM square microcavity laser, HSRL laser, and HSRRL laser. Additionally, we packaged and characterized HSRRL lasers at the module level. A systematic account of the evolution and development of these coupled-cavity lasers was presented. The hybrid cavity structure consisting of a WGM cavity and an FP cavity is a feasible and cost-effective method to fabricate a single-mode semiconductor laser with efficient unidirectional emission, high Q factor, and tunable wavelength. The characteristics of the hybrid mode in the HSRL were analyzed by simulation, and stable single-mode lasing was realized experimentally. The HSRRL was modified from the HSRL, and its fundamental transverse mode fraction in the FP cavity was improved from 35% to 91%, leading to a higher coupling efficiency to an SMF. The HSRRL was packaged in a hermetic box-can with a coupling efficiency of 47% for the SMF, and was tested at the module level. This study represents the first attempt at the industrialization of an HSRRL. The TOSA, which was based on the HSRRL chip, has a wide and continuous wavelength tuning range that is expected to encompass C-band DWDM specifications. During wavelength switching, the TOSA operated in a favorable single-mode state, demonstrating SMSRs greater than 35 dB, along with satisfactory output power suitable for various applications.

Compared with traditional optical transmitter devices, the TOSA based on an HSRRL has the advantages of a compact structure, simple fabrication process, stable single-mode emission, simple tuning mechanism, and wide continuous tuning range, which meet the requirements of next-generation communication technology, including DWDM, NGPON2, and coherent optical communication. We expect that such a device can be improved to be more reliable, and be commercialized and industrialized for large-scale production in the future.

Author Contributions: Conceptualization, Y.-Z.H. (Yong-Zhen Huang), J.-L.X. and Y.-D.Y.; methodology, Y.-Z.H. (Yong-Zhen Huang), Y.-D.Y. and A.L.T.; software, M.-Q.W., B.Z., Y.-Z.H. (You-Zeng Hao) and Z.-N.Z.; validation, M.-Q.W. and B.Z.; formal analysis, B.Z.; investigation, M.-Q.W. and B.Z.; resources, J.-L.X., Z.-N.Z. and Y.-Z.H. (You-Zeng Hao); data curation, B.Z. and Z.-H.H.; writing—original draft preparation, M.-Q.W., J.-L.X. and B.Z.; writing—review and editing, J.-L.X. and A.L.T.; visualization, M.-Q.W., Z.-N.Z. and B.Z.; supervision, Y.-Z.H. (Yong-Zhen Huang) and

J.-L.X.; project administration, J.-L.X. and B.Z. All authors have read and agreed to the published version of the manuscript.

Institutional Review Board Statement: Not applicable.

Informed Consent Statement: Not applicable.

Data Availability Statement: Data are contained within the article.

Conflicts of Interest: Author Miao-Qing Wang and Bin Zhang was employed by the company Shaoxing ZKTEL Equipment Co., Ltd. The remaining authors declare that the research was conducted in the absence of any commercial or financial relationships that could be construed as a potential conflict of interest.

References

1. Wang, X.X.; Li, Z.X.; Wang, R.; Zhu, G.Y.; Qin, F.F.; Chen, J.P.; Wang, J.J.; Shi, Z.L.; Cui, Q.N.; Xu, C.X. Electrically driven optical resonance of spherical ZnO whispering gallery mode microcavity. *Appl. Phys. Lett.* **2021**, *119*, 021101. [CrossRef]
2. Shi, L.L.; Wang, Q.Q.; Jiang, L.D.; Gao, Q.R.; Zhu, T. In-Fiber Butt-Coupled Spherical Microcavity with Whispering Gallery Mode and Fabry-Perot Resonances. *IEEE Photonics Technol. Lett.* **2021**, *33*, 553–556. [CrossRef]
3. Drechsler, M.L.; Choi, L.S.M.; Tabataba-Vakili, F.; Nippert, F.; Koulas-Simos, A.; Lorke, M.; Reitzenstein, S.; Alloing, B.; Boucaud, P.; Wagner, M.R.; et al. Multimode Emission in GaN Microdisk Lasers. *Laser Photon. Rev.* **2024**, *18*, 2400221. [CrossRef]
4. De Oliveira, R.; Colombano, M.; Malabat, F.; Morassi, M.; Lemaitre, A.; Favero, I. Whispering-Gallery Quantum-Well Exciton Polaritons in an Indium Gallium Arsenide Microdisk Cavity. *Phys. Rev. Lett.* **2024**, *132*, 126901. [CrossRef]
5. Kryzhanovskaya, N.V.; Ivanov, K.A.; Fominykh, N.A.; Komarov, S.D.; Makhov, I.S.; Moiseev, E.I.; Guseva, J.A.; Kulagina, M.M.; Mintairov, S.A.; Kalyuzhnyy, N.A.; et al. III-V microdisk lasers coupled to planar waveguides. *J. Appl. Phys.* **2023**, *134*, 103101. [CrossRef]
6. Mao, M.H.; Chien, H.C.; Hong, J.Z.; Cheng, C.Y. Room-temperature low-threshold current-injection InGaAs quantum-dot microdisk lasers with single-mode emission. *Opt. Express* **2011**, *19*, 14145–14151. [CrossRef]
7. Mohideen, U.; Hobson, W.S.; Pearton, S.J.; Ren, F.; Slusher, R.E. GaAs/AlGaAs Microdisk Lasers. *Appl. Phys. Lett.* **1994**, *64*, 1911–1913. [CrossRef]
8. Kryzhanovskaya, N.V.; Moiseev, E.I.; Nadtochiy, A.M.; Melnichenko, I.A.; Fominykh, N.A.; Ivanov, K.A.; Komarov, S.D.; Makhov, I.S.; Lutsenko, E.V.; Vainilovich, A.G.; et al. Output Power of III-V Injection Microdisk and Microring Lasers. *IEEE J. Sel. Top. Quantum Electron.* **2025**, *31*, 1501312. [CrossRef]
9. Wang, J.W.; Li, X.; Guo, X.; Loh, T.; Ranno, L.; Liu, C.Y.; Rusli; Wang, H.; Sia, J.X.B. Scalable single-microring hybrid III-V/Si lasers for emerging narrow-linewidth applications. *Opt. Express* **2024**, *32*, 26751–26762. [CrossRef]
10. Liang, D.; Fiorentino, M.; Okumura, T.; Chang, H.H.; Spencer, D.T.; Kuo, Y.H.; Fang, A.W.; Dai, D.; Beausoleil, R.G.; Bowers, J.E. Electrically-pumped compact hybrid silicon microring lasers for optical interconnects. *Opt. Express* **2009**, *17*, 20355–20364. [CrossRef]
11. Yang, Y.D.; Huang, Y.Z. Mode characteristics and directional emission for square microcavity lasers. *J. Phys. D-Appl. Phys.* **2016**, *49*, 253001. [CrossRef]
12. McCall, S.L.; Levi, A.F.J.; Slusher, R.E.; Pearton, S.J.; Logan, R.A. Whispering-Gallery Mode Microdisk Lasers. *Appl. Phys. Lett.* **1992**, *60*, 289–291. [CrossRef]
13. Levi, A.F.J.; Slusher, R.E.; McCall, S.L.; Pearton, S.J.; Hobson, W.S. Room-Temperature Lasing Action In $In_{0.51}Ga_{0.49}P/In_{0.2}Ga_{0.8}As$ Microcylinder Laser-Diodes. *Appl. Phys. Lett.* **1993**, *62*, 2021–2023. [CrossRef]
14. Slusher, R.E.; Levi, A.F.J.; Mohideen, U.; McCall, S.L.; Pearton, S.J.; Logan, R.A. Threshold Characteristics of Semiconductor Microdisk Lasers. *Appl. Phys. Lett.* **1993**, *63*, 1310–1312. [CrossRef]
15. Koch, S.W.; Jahnke, F.; Chow, W.W. Physics of Semiconductor Microcavity Lasers. *Semicond. Sci. Technol.* **1995**, *10*, 739–751. [CrossRef]
16. Fujita, M.; Inoshita, K.; Baba, T. Room temperature continuous wave lasing characteristics of GaInAsP/InP microdisk injection laser. *Electron. Lett.* **1998**, *34*, 278–279. [CrossRef]
17. Choi, S.J.; Djordjev, K.; Choi, S.J.; Dapkus, P.D. Microdisk lasers vertically coupled to output waveguides. *IEEE Photonics Technol. Lett.* **2003**, *15*, 1330–1332. [CrossRef]
18. Kazes, M.; Lewis, D.Y.; Banin, U. Method for preparation of semiconductor quantum-rod lasers in a cylindrical microcavity. *Adv. Funct. Mater.* **2004**, *14*, 957–962. [CrossRef]
19. Gies, C.; Wiersig, J.; Lorke, M.; Jahnke, F. Semiconductor model for quantum-dot-based microcavity lasers. *Phys. Rev. A* **2007**, *75*, 013803. [CrossRef]
20. Tamboli, A.C.; Haberer, E.D.; Sharma, R.; Lee, K.H.; Nakamura, S.; Hu, E.L. Room-temperature continuous-wave lasing in GaN/InGaN microdisks. *Nat. Photonics* **2007**, *1*, 61–64. [CrossRef]

21. Yan, C.L.; Wang, Q.J.; Diehl, L.; Hentschel, M.; Wiersig, J.; Yu, N.F.; Pflügl, C.; Capasso, F.; Belkin, M.A.; Edamura, T.; et al. Directional emission and universal far-field behavior from semiconductor lasers with limaccedilon-shaped microcavity. *Appl. Phys. Lett.* **2009**, *94*, 251101. [CrossRef]

22. Jiang, X.F.; Xiao, Y.F.; Zou, C.L.; He, L.N.; Dong, C.H.; Li, B.B.; Li, Y.; Sun, F.W.; Yang, L.; Gong, Q.H. Highly Unidirectional Emission and Ultralow-Threshold Lasing from On-Chip Ultrahigh-Q Microcavities. *Adv. Mater.* **2012**, *24*, OP260–OP264. [CrossRef] [PubMed]

23. Wang, D.Q.; Zhu, T.T.; Oliver, R.A.; Hu, E.L. Ultra-low-threshold InGaN/GaN quantum dot micro-ring lasers. *Opt. Lett.* **2018**, *43*, 799–802. [CrossRef] [PubMed]

24. Yang, Y.D.; Wang, S.J.; Huang, Y.Z. Investigation of mode coupling in a microdisk resonator for realizing directional emission. *Opt. Express* **2009**, *17*, 23010–23015. [CrossRef]

25. Song, Q.H.; Ge, L.; Stone, A.D.; Cao, H.; Wiersig, J.; Shim, J.B.; Unterhinninghofen, J.; Fang, W.; Solomon, G.S. Directional Laser Emission from a Wavelength-Scale Chaotic Microcavity. *Phys. Rev. Lett.* **2010**, *105*, 103902. [CrossRef]

26. Wiersig, J.; Hentschel, M. Combining directional light output and ultralow loss in deformed microdisks. *Phys. Rev. Lett.* **2008**, *100*, 033901. [CrossRef]

27. Chern, G.D.; Tureci, H.E.; Stone, A.D.; Chang, R.K.; Kneissl, M.; Johnson, N.M. Unidirectional lasing from InGaN multiple-quantum-well spiral-shaped micropillars. *Appl. Phys. Lett.* **2003**, *83*, 1710–1712. [CrossRef]

28. Boriskina, S.V.; Benson, T.M.; Sewell, P.; Nosich, A.I. Q factor and emission pattern control of the WG modes in notched microdisk resonators. *IEEE J. Sel. Top. Quantum Electron.* **2006**, *12*, 52–58. [CrossRef]

29. Tsang, W.T.; Olsson, N.A.; Logan, R.A. High-Speed Direct Single-Frequency Modulation with Large Tuning Rate and Frequency Excursion in Cleaved-Coupled-Cavity Semiconductor-Lasers. *Appl. Phys. Lett.* **1983**, *42*, 650–652. [CrossRef]

30. He, J.J.; Liu, D. Wavelength switchable semiconductor laser using half-wave V-coupled cavities. *Opt. Express* **2008**, *16*, 3896–3911. [CrossRef]

31. Gong, J.L.; Wang, Z.Y.; He, J.J.; Li, L.; Yang, R.Q.; Gupta, J.A. Single-mode interband cascade laser based on V-coupled cavity with 210 nm wavelength tuning range near 3 μm. *Opt. Express* **2023**, *31*, 38409–38418. [CrossRef] [PubMed]

32. Liu, B.; Shakouri, A.; Bowers, J.E. Wide tunable double ring resonator coupled lasers. *IEEE Photonics Technol. Lett.* **2002**, *14*, 600–602. [CrossRef]

33. Shang, L.; Liu, L.Y.; Xu, L. Single-frequency coupled asymmetric microcavity laser. *Opt. Lett.* **2008**, *33*, 1150–1152. [CrossRef]

34. Phelan, R.; Guo, W.-H.; Lu, Q.; Byrne, D.; Roycroft, B.; Lambkin, P.; Corbett, B.; Smyth, F.; Barry, L.P.; Kelly, B.; et al. A novel two-section tunable discrete mode Fabry-Perot laser exhibiting nanosecond wavelength switching. *IEEE J. Quantum Electron.* **2008**, *44*, 331–337. [CrossRef]

35. D'Agostino, D.; Lenstra, D.; Ambrosius, H.; Smit, M.K. Coupled cavity laser based on anti-resonant imaging via multimode interference. *Opt. Lett.* **2015**, *40*, 653–656. [CrossRef]

36. Ma, X.W.; Huang, Y.Z.; Yang, Y.D.; Xiao, J.L.; Weng, H.Z.; Xiao, Z.X. Mode coupling in hybrid square-rectangular lasers for single mode operation. *Appl. Phys. Lett.* **2016**, *109*, 071102. [CrossRef]

37. Xu, R.; Deng, C.S. New protection solution in native passive O-band CWDM for 5G front-haul. *Telecom Eng. Tech. Stand.* **2019**, *32*, 1–6. [CrossRef]

38. Zhang, H.; Huang, W.P. Product Definition and Enabling Technologies for Product Definition and Enabling Technologies for 5G Wireless Transceiver. *ZTE Technol. J.* **2018**, *24*, 51–53. [CrossRef]

39. Zhang, L.; Luo, Y.Q.; Ansari, N.; Gao, B.; Liu, X.; Effenberger, F. Enhancing Next Generation Passive Optical Network Stage 2 (NG-PON2) with Channel Bonding. In Proceedings of the 12th International Conference on Networking, Architecture, and Storage (NAS), Shenzhen, China, 7–9 August 2017; pp. 202–207.

40. Hawthorn, C.J.; Weber, K.P.; Scholten, R.E. Littrow configuration tunable external cavity diode laser with fixed direction output beam. *Rev. Sci. Instrum.* **2001**, *72*, 4477–4479. [CrossRef]

41. Ishii, H.; Kasaya, K.; Oohashi, H.; Shibata, Y.; Yasaka, H.; Okamoto, K. Widely wavelength-tunable DFB laser array integrated with funnel combiner. *IEEE J. Sel. Top. Quantum Electron.* **2007**, *13*, 1089–1094. [CrossRef]

42. Ward, A.J.; Robbins, D.J.; Busico, G.; Barton, E.; Ponnampalam, L.; Duck, J.P.; Whitbread, N.D.; Williams, P.J.; Reid, D.C.J.; Carter, A.C.; et al. Widely tunable DS-DBR laser with monolithically integrated SOA: Design and performance. *IEEE J. Sel. Top. Quantum Electron.* **2005**, *11*, 149–156. [CrossRef]

43. Caponio, N.P.; Goano, M.; Maio, I.; Meliga, M.; Bava, G.P.; Destefanis, G.; Montrosset, I. Analysis and Design Criteria of 3-Section DBR Tunable Lasers. *IEEE J. Sel. Areas Commun.* **1990**, *8*, 1203–1213. [CrossRef]

44. Hao, Y.Z.; Wang, F.L.; Tang, M.; Weng, H.Z.; Yang, Y.D.; Xiao, J.L.; Huang, Y.Z. Widely tunable single-mode lasers based on a hybrid square/rhombus-rectangular microcavity. *Photonics Res.* **2019**, *7*, 543–548. [CrossRef]

45. Wang, M.Q.; Hao, Y.Z.; Zhang, Z.N.; Zhang, B.; Yang, Y.D.; Xiao, J.L.; Teixeira, A.L.; Huang, Y.Z. Directly Modulated Tunable Single-Mode Lasers Based on a Coupled Microcavity. *Photonics* **2022**, *9*, 827. [CrossRef]

46. Liu, J.C.; Huang, Y.Z.; Hao, Y.Z.; Fan, Y.R.; Wu, J.L.; Yang, K.; Xiao, J.L.; Yang, Y.D. Relative Intensity Noise and Linewidth for Hybrid-Cavity Semiconductor Lasers. *J. Lightwave Technol.* **2022**, *40*, 2087–2096. [CrossRef]
47. Hao, Y.Z.; Sheng, M.W.; Zhang, Z.N.; Li, J.C.; Xiao, J.L.; Yang, Y.D.; Huang, Y.Z. High-Speed Directly Modulated Widely Tunable Hybrid Square/Rhombus-Rectangular Coupled Cavity Lasers. *J. Lightwave Technol.* **2023**, *41*, 5668–5674. [CrossRef]